Molecular dynamics simulations of the effects of vacancies on nickel self-diffusion, oxygen diffusion and oxidation initiation in nickel, using the ReaxFF reactive force field

5 AUTHORS, INCLUDING:

Chenyu Zou
Pennsylvania State University
11 PUBLICATIONS **68** CITATIONS

SEE PROFILE

Yun Kyung Shin
Pennsylvania State University
20 PUBLICATIONS **156** CITATIONS

SEE PROFILE

Adri C.T. van Duin
Pennsylvania State University
361 PUBLICATIONS **8,207** CITATIONS

SEE PROFILE

Huazhi Fang
University of Science and Technology Beijing
25 PUBLICATIONS **247** CITATIONS

SEE PROFILE

Molecular dynamics simulations of the effects of vacancies on nickel self-diffusion, oxygen diffusion and oxidation initiation in nickel, using the ReaxFF reactive force field

Chenyu Zou,[a] Yun Kyung Shin,[a] Adri C.T. van Duin,[a,*] Huazhi Fang[b] and Zi-Kui Liu[b]

[a]Department of Mechanical and Nuclear Engineering, The Pennsylvania State University, University Park, PA 16802, USA
[b]Department of Materials Science and Engineering, The Pennsylvania State University, University Park, PA 16802, USA

Abstract—A ReaxFF reactive force field was developed for the nickel–oxygen system. The quantum mechanical (QM) data used to derive the force field parameters included the equations of state of various phases of nickel and that of nickel oxide (NiO), the vacancy formation energy and the vacancy-mediated self-diffusion barrier in the face-centered cubic nickel. Furthermore, in order to study the interstitial diffusion of oxygen atoms in the nickel matrix, the oxygen insertion energies and the diffusion barriers were included in the training set. The force field was validated by performing molecular dynamics (MD) simulations of self-diffusion of nickel and the interstitial diffusion of oxygen. The predicted diffusivity and the activation energy achieved quantitative agreement with their respective published values. Furthermore, this force field enables study of the effects of vacancies on the diffusion of dissolved oxygen and the successive initiation of internal oxidation. A new oxygen diffusion mechanism is proposed in which the oxygen atom diffuses via the movement of the oxygen–vacancy pair. In addition, the MD simulation results suggest that the voids at the grain boundaries can induce local oxygen segregation due to the strong oxygen–vacancy binding effect, which is responsible for the formation of a nickel oxide particle in the void. These results demonstrate that the ReaxFF MD study can contribute to bridging the gap between the QM calculations and the experimental observations in the study of metal oxidation.
© 2014 Acta Materialia Inc. Published by Elsevier Ltd. All rights reserved.

Keywords: Molecular dynamics; ReaxFF; Vacancy; Diffusion; Oxidation

1. Introduction

Nickel-based superalloys are applied in the energy industry [1–3] under extreme conditions such as high temperatures in conjunction with a corrosive environment. Compared with other metals, these materials exhibit good mechanical strength and resistance to corrosion at high temperatures [4]. Although such nickel-based superalloys have been studied extensively for many decades, there is still significant discussion regarding the fundamental oxidation mechanism of these materials [5].

The oxygen diffusion process is of great importance, because this process is at the origin of alloy oxidation and is partially responsible for the deterioration of the mechanical properties of metallic materials [6–8]. Several experimental techniques ([9], and the references therein) have been employed to measure the solubility and diffusivity of oxygen. Such techniques include internal oxidation, electron-stimulated desorption, electrochemical techniques and secondary ion mass spectrometry. However, the measured values for the diffusivity and the activation

energy were found to be scattered over a wide range. Such uncertainties indicate large errors associated with these experimental studies.

Besides the experimental efforts in determining the diffusivity of oxygen in nickel, theoretical investigations have also been carried out on the subject using first-principles calculations. These calculations can determine the thermodynamic properties of materials and the kinetic parameters of chemical processes based on fundamental knowledge of the electronic structures. In the case of the interstitial diffusion of an oxygen atom in a dilute solid solution, the solution energy of an oxygen atom as well as the diffusion barrier can be obtained by performing first-principles calculations using relevant molecular models. In these calculations, the diffusivity is assumed to scale linearly with the jumping rate, which depends on the activation energy of each jump [10]. Previous calculations [11,12] have not considered the vacancy effect, and therefore underestimated the activation energy of diffusion. Recent studies [13,14] have demonstrated improved agreement with experimental observations by considering the effect of vacancies on oxygen diffusion. It has been shown that the strong binding effect between the oxygen atoms and vacancies will significantly increase the activation energy of the diffusion process and therefore decrease the mobility of interstitial oxygen atoms.

---

* Corresponding author. Tel.: +1 814 863 6277; e-mail: acv13@psu.edu

However, the diffusion of oxygen during the oxidation process of nickel is much more complicated than interstitial diffusion. Perusin et al. [9] demonstrated that the grain-boundary (GB) diffusion of oxygen could play an important role in the oxidation of nickel. This short-circuit diffusion pathway could potentially lead to the formation of nickel oxide inside the voids of GB. First-principles calculations have difficulties describing these diffusion and oxidation phenomena at GB, because a large number of atoms are required to model the complex local environment of GB. The length scale of such a model is beyond the capability of quantum mechanical (QM) methods within reasonable computational cost. Furthermore, most of the QM calculations explore the potential energy surface of a particular system at 0 K. Thus, the dynamics of a system containing multiple atoms at high temperature such as the metal oxidation process are largely unaccounted for. First-principles molecular dynamics (MD) methods [15] have been employed to address this issue. However, the system scale and the time span of these simulations are highly restricted (~100 atoms and several picoseconds, respectively), owing to the time-consuming electronic structure calculations.

To account for the gap (in both length and time scale) between experimental observations and theoretical calculations, simplified/empirical potentials have been developed and employed in MD simulations to predict material properties and to study their behavior at elevated temperatures. In these simplified potentials, the electronic degrees of freedom are frozen, and the interatomic interaction is described by empirical functions. Owing to their empirical nature, these functions contain parameters that need to be optimized against results obtained from higher levels of theory or experiments. The resulting potential can reproduce the potential energy surface within a certain accuracy, and hence be used to study static optimized geometry [16] and to explore system dynamics at high temperatures at a lower computational cost than the first-principles approach. In the case of metallic systems, the well-known embedded atom method (EAM) [17] is widely used in studying various properties and processes of both pure metals and multi-metallic alloy systems [18]. Hayat et al. [19] extensively studied the thermal properties of nickel metal using the EAM.

Despite its great success in providing a theoretical description of metallic systems, the EAM finds difficulties in simulating the oxidation phenomenon, because the potential function lacks the capability of describing the dynamic charge transfer between oxygen and metal atoms as well as the coulomb interactions between the resulting ions and cations. To address this issue, Zhou et al. [20] developed a charge-transfer ionic embedded atom potential that adds an extra energy term to the non-ionic energy terms of the EAM potential. The resulting potential features an electrostatic contribution and can be used to study the metal oxidation phenomenon. Variable charge molecular dynamics (VCMD) simulations of metal oxidation using this potential have been widely carried out on metallic systems such as nano-crystalline [21] and single-crystal [22] forms of aluminum, nickel–aluminum alloy [23] and the iron–aluminum–nickel ternary alloy system [24]. Specifically for the nickel–oxygen system, Garruchet et al. [25] studied the initial stage of oxidation on three different surfaces of nickel metal. The predicted oxygen surface coverage before the initiation of nucleation of surface oxide islands showed good agreement with experimental observations. In addition, the authors used this method to describe

the interstitial diffusion of oxygen in the presence of lattice vacancies [26]. Furthermore, Elsener et al. [27] proposed a new charge optimization approach within the framework of VCMD that can significantly enhance the original potential in terms of computational savings. The authors have further applied the resulting variable-charge method in studying GB migration in the presence of interstitial oxygen atoms using a GB model containing ~30,000 atoms [28].

In the current study, a ReaxFF [29] description of the Ni/O system was developed. The motivation of this work lies in the demonstrated higher accuracy of ReaxFF in describing diffusion phenomena in a single metallic system compared with that of the EAM potential [30]. In addition, ReaxFF features a charge calculation scheme (the Electronegativity Equalization Method [31], which is shielded for excessively high repulsion at close range [32]) that is similar to the charge transfer ionic model used in VCMD simulations [33]. This feature enables ReaxFF to describe the oxidation of metals. Furthermore, the formulation of the ReaxFF potential ensures the extension of the parameter set to more complex systems involving species other than O_2 molecules (e.g. H_2 and H_2O) that can be observed in a typical corrosive environment. For example, Russo and co-workers [34] reported a MD study on the use of the ReaxFF potential to model the interaction between aluminum clusters and water molecules. The transferability of the potential has been demonstrated by many successful applications of ReaxFF in describing covalent [35,36], metallic [37–40], ionic metal hydride [41–45] and metal oxide [46–48] materials. MD simulations employing the ReaxFF potential have been widely used to study the detailed chemical mechanisms related to scientific phenomena such as combustion [49–51], pyrolysis [52–57], catalysis [58–60], high-energy atomic collisions [61] and the processes undergone by nano-materials [62–64].

In the present work, the QM method used to generate data for force field fitting is briefly discussed. These QM data were reported in a recent publication [13] concerning the bulk diffusion of oxygen in nickel. The theoretically calculated oxygen diffusivity in the presence of a nearby vacancy based on QM data is supported by MD simulations using both the ReaxFF and the modified EAM potential. However, the diffusivity predicted using the ReaxFF potential was based on small systems (256 nickel atoms) and was associated with relatively large errors both in the diffusivity and in the activation energy. The present study systematically presents force field parameterization results related to the Ni/O system and the diffusivity studies involving larger systems, thus reducing the effects of size on the diffusivity. Multiple simulations are performed to measure the errors associated with the diffusivity predicted from MD simulations. Furthermore, a new oxygen diffusion mechanism is proposed based on the results of the MD simulations, as will be discussed in the following sections. Lastly, the force field is used to study the initial stage of vacancy-induced internal oxidation in nickel.

2. Computational methods

2.1. QM methods

QM methods for calculating the equations of state (EOS) of five types of crystal structure exhibited by nickel have been described in previous studies [38,59]. A similar

approach is used to calculate the EOS of NiO, as described in Ref. [65]. Other first-principles data, as mentioned in the following sections, are calculated using the Vienna Ab initio Simulation Package (VASP) [66,67]. The extension of the original data set [59,65] improves the ReaxFF description of nickel metal, as will be demonstrated in the following sections. The electron–ion interactions are described by the projector-augmented-wave method [68], and the exchange and correlation are treated within the local density approximation (LDA) [69]. The electron orbital is expanded over a plane-wave basis set with a kinetic energy cut-off of 520 eV. The Brillouin zone is sampled using a Monkhorst–Pack scheme with a $7 \times 7 \times 7$ k-point mesh. Other detailed calculation schemes are described by Fang et al. [13].

2.2. ReaxFF reactive force field

ReaxFF is a bond-order-based [70,71] potential in which the system energy receives contributions from bonded and non-bonded interactions. The bonded interactions (chemical bonds, valence angles and torsion angles) are bond-order-dependent, with the bond order itself being calculated based on interatomic distances. In the current Ni/O description, torsion angles are not included in the potential. The non-bonded interactions (van der Waals and Coulomb) are calculated between each pair of atoms in the system, regardless of connectivity with a distance cut-off of 10 Å. These interactions are shielded for excessively high repulsion at short distances. By optimizing the relevant parameter sets against QM results and experimental measurements, the ReaxFF potential attempts to reproduce the energetics (thermodynamics as well as reaction barriers) of relevant materials with QM-level accuracy, while maintaining orders of magnitude lower computational costs compared with ab initio methods when applied to large systems. The parallel implementation of the ReaxFF potential enables MD simulations at elevated temperatures involving large numbers of particles ($\sim 10^6$ atoms [72,73]) for durations of up to several nanoseconds. A recent study [74] extended this time duration to the microsecond time scale by coupling the ReaxFF potential with parallel replica dynamics methods, as implemented in the LAMMPS [75] package. A detailed description of the functional forms of the ReaxFF potential can be found in Ref. [29]. The force field parameterization uses the single-parameter optimization approach described in Ref. [76].

2.3. MD simulations for diffusion

Vacancy-mediated self-diffusion of nickel was modeled using a nickel face-centered cubic (fcc) super cell with a number of nickel atoms removed to create suitable vacancy concentrations. Interstitial oxygen diffusion was modeled by inserting one oxygen atom in a $6 \times 6 \times 6$ nickel super cell. The system was chosen to be large enough to eliminate the effect of system size. The diffusion of oxygen atoms under the effects of vacancies was modeled by placing one oxygen atom at an octahedral site near a removed nickel atom (i.e. vacancy). All the systems were equilibrated using an NPT (constant number of particles, constant zero pressure and constant temperature) ensemble for 5 ps for sufficient lattice relaxation at the corresponding temperature. After the equilibration stage, the MD simulation was restarted from the end of the NPT trajectory with the

ensemble switched to NVE (constant number of particles, volume and energy). The diffusion coefficient was then calculated using Einstein's relation [77], $D = \frac{\langle (R_t - R_0)^2 \rangle}{6t}$, where D denotes the three-dimensional diffusion coefficient, R_t denotes the position of a corresponding atom at time t, and R_0 denotes the initial position. The MSD was calculated by averaging a series of R_t values over at least 1 ns. The time step in all the simulations was 0.25 fs, with the temperature and pressure controlled, if applicable, by a Berendsen thermostat [78] and a barostat with damping constants of 100 and 3000 fs, respectively.

3. Results and discussion

3.1. Force field development

3.1.1. Nickel–nickel interaction

The initial ReaxFF parameters for nickel are adopted from previous work [59]. Owing to the extension of the training data pertaining to the vacancy formation energy and the diffusion barrier, a systematic improvement in the description of nickel metal is achieved compared with previous results. The new nickel metal description afforded by ReaxFF is shown in Table 1, where the values of key parameters are listed. The EOS of five different nickel crystal structures are used to parameterize the force field, as demonstrated in Fig. 1. Although many of these crystal structures are not experimentally obtainable, theoretical calculations using the QM method are feasible for these structures and are useful during the force-field training process, because it is essential for the force field to recognize these structures as energetically unfavorable and to avoid them during MD simulations at high temperatures. The formation energies of the body-centered cubic, A15, simple cubic and diamond crystal structures predicted by ReaxFF are 0.8 kcal mol^{-1}, 2.8 kcal mol^{-1}, 18.6 kcal mol^{-1} and 29.7 kcal mol^{-1} higher than the energy of the fcc structure, whereas the QM data are 0.9 kcal mol^{-1}, 2.7 kcal mol^{-1}, 15.0 kcal mol^{-1} and 30.2 kcal mol^{-1} higher, respectively. The equilibrium lattice constant for the fcc nickel crystal structure is 3.511 Å, which is in better agreement with the QM value of 3.521 Å and the experimentally measured value of 3.524 Å [79] than the values reported in previous work.

The surface formation energies for fcc (100) and fcc (111) surfaces are predicted by ReaxFF to be 15.6 kcal mol^{-1} and 12.1 kcal mol^{-1}, respectively, which are in good agreement with the QM values of 18.9 kcal mol^{-1} and 14.1 kcal mol^{-1}. Both surface energies agree well with the experimentally measured values of 14.1 kcal mol^{-1} [80] and 18.4 kcal mol^{-1} [81], respectively. Nevertheless, a contradictory prediction is observed between the first-principles calculation and the experimental prediction regarding the relative stability of the two surfaces. It was chosen to fit the trend from the QM prediction because fcc (111) is the most compact surface of the fcc crystal structure and is therefore expected to be more stable than the fcc (100) surface.
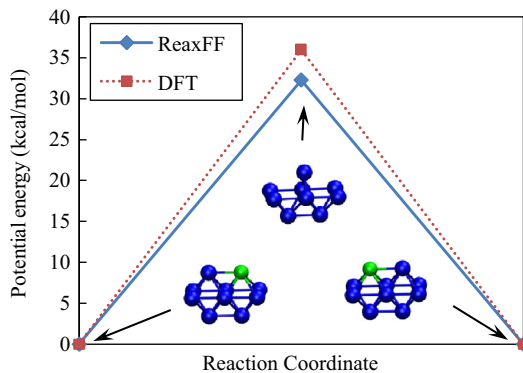
The nickel vacancy formation energy is predicted to be 45.0 kcal mol^{-1} using a $2 \times 2 \times 2$ super cell, higher than the QM value of 38.7 kcal mol^{-1}. Previous theoretical and experimental predictions of this energy ranged from 29.5 kcal mol^{-1} to 41.7 kcal mol^{-1} [82]. The vacancy

Table 1. Values of key parameters of the ReaxFF description of nickel (r_0^σ and r_{vdW} in Å; E_{vdW} and D_e^σ in kcal/mol; all other parameters are unitless).

Atom	r_0^σ	r_{vdW}	E_{vdW}	γ_{EEM}	α	γ_w
Ni	1.8244	1.8442	0.1840	0.8105	12.3227	3.8387
Bond	D_e^σ	$p_{be,1}$	$p_{ovun,1}$	$p_{be,2}$	$p_{bo,1}$	$p_{bo,2}$
Ni–Ni	90.1410	−0.3857	0.3225	1.0927	−0.1027	4.6972
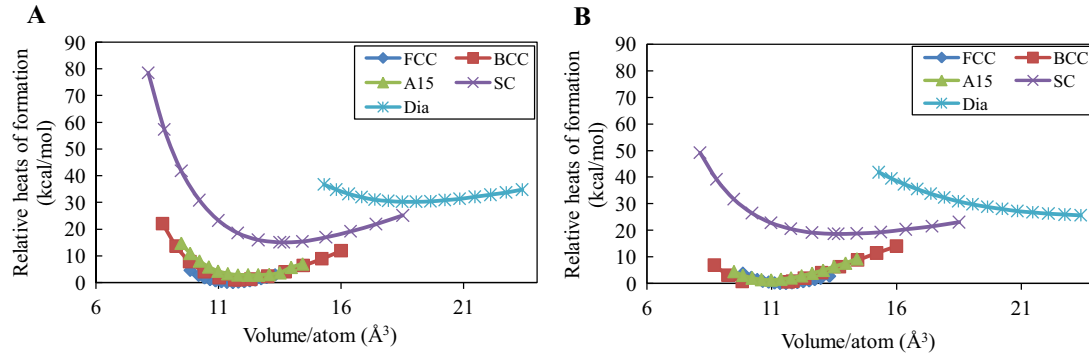
Fig. 1. Comparison of the predicted EOS between (A) QM and (B) ReaxFF for five different crystal structures of nickel.

migration barrier predicted by ReaxFF is 32.3 kcal mol^{-1}, which compares well with the QM value of 36.0 kcal mol^{-1} as demonstrated in Fig. 2. Other theoretical predictions of this value range from 26.5 kcal mol^{-1} to 41.7 kcal mol^{-1}, depending on whether or not the structure is fully relaxed as well as on the size of the super cell used in the model. The current ReaxFF potential predicts the vacancy formation energy ranging from 45.0 kcal mol^{-1} for a $2 \times 2 \times 2$ super cell to 38.7 kcal mol^{-1} for a $4 \times 4 \times 4$ super cell and larger cells. With respect to the vacancy diffusion barrier, the ReaxFF predicts a value of 32.3 kcal mol^{-1} for a $2 \times 2 \times 2$ super cell and 38.1 kcal mol^{-1} for an $8 \times 8 \times 8$ super cell. In these two cases (the vacancy formation energy and the diffusion barrier), relatively large discrepancies (an absolute value of ~7 kcal mol^{-1}) are observed between the results predicted from different exchange and correlation functional forms within the framework of density functional theory. The ReaxFF value is trained to reproduce the LDA value because of the demonstrated higher accuracy of LDA over GGA in describing systems involving vacancies [83], while maintaining equally satisfactory results for the bulk and surface properties.

3.1.2. Nickel–oxygen interaction

Data included in the force-field fitting for the Ni–O interaction pertain mainly to interstitial insertion energies and diffusion barriers. The relative heats of formation of NiO at various densities (Fig. 3) are also included to further facilitate the development of the force field and describe a nickel oxide system containing a high oxygen concentration. Recent theoretical studies [13,14] demonstrated the strong binding effect between the oxygen atoms and the lattice vacancies. Thus, energies related to the presence of a vacancy (the insertion energy and the diffusion barrier) are also included in the force-field fitting procedure. The optimized parameters are listed in Table 2. The oxygen insertion energies in the absence of vacancies are predicted to be 21.7 kcal mol^{-1} and 13.9 kcal mol^{-1} at octahedral and tetrahedral sites, respectively. These values agree well with the corresponding QM values of 24.2 kcal mol^{-1} and 16.1 kcal mol^{-1}. In the presence of a vacancy, the insertion energies at the two sites increase to 47.4 kcal mol^{-1} and 18.5 kcal mol^{-1}, which compare well with the QM predictions of 47.5 kcal mol^{-1} and 19.1 kcal mol^{-1}. The stability of an interstitial oxygen atom is enhanced by up to ~20 kcal mol^{-1} at octahedral sites, owing to the vacancy effect. A similar effect is predicted for the diffusion barriers. Two classical interstitial diffusion pathways are considered:
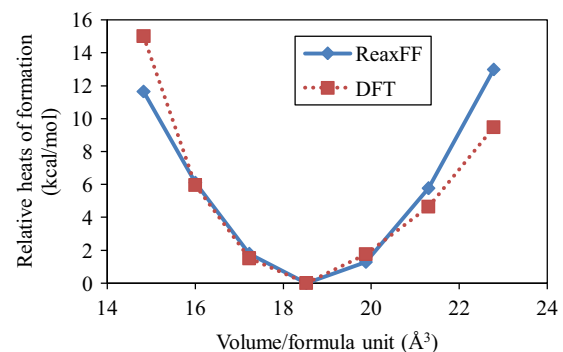

Fig. 2. ReaxFF fit for the nickel vacancy migration pathway. Color code: blue, nickel atom; green, vacancy. (For interpretation of the references to color in this figure legend, the reader is referred to the online version of this article.)

Fig. 3. ReaxFF fit for the EOS of NiO.

Table 2. Values of key parameters of the ReaxFF description of the Ni–O interaction (E_{dis} in kcal/mol; r_0^σ in Å; Θ_0 in deg; all other parameters are unitless).

Bond	D_e^σ	$p_{be,1}$	$p_{be,2}$	$p_{bo,3}$	$p_{bo,4}$	$p_{bo,1}$	$p_{bo,2}$
O–Ni	86.9034	0.3377	2.5302	-0.2500	15.0000	1.0000	16.0000
Off-diagonal	E_{dis}	r_{vdW}	α		r_0^σ		
O–Ni	0.0514	1.7820	12.8150		1.4000		
Angle	Θ_0	k_a	k_b	$p_{v,1}$		$p_{v,2}$	
O–O–Ni	81.5303	14.3201	4.2643	0.3854		2.4644	
O–Ni–O	33.8130	15.1818	4.0000	0.0354		1.3198	
Ni–O–Ni	88.1216	15.8581	2.7094	0.6326		1.1340	
O–Ni–Ni	19.7429	2.9501	3.6277	0.0732		1.7069	

octahedral–tetrahedral (O–T) jumps and octahedral–octahedral (O–O) jumps, as demonstrated in Fig. 4. The presence of vacancies increases the diffusion barriers by $\sim$10 kcal mol^{-1} (from 22.0 kcal mol^{-1} to 31.2 kcal mol^{-1}, and the QM value increases from 21.5 kcal mol^{-1} to 31.4 kcal mol^{-1}) and $\sim$20 kcal mol^{-1} (from 33.0 kcal mol^{-1} to 53.4 kcal mol^{-1}, and the QM value increases from 32.3 kcal mol^{-1} to 53.0 kcal mol^{-1}) for the two diffusion pathways, respectively, compared with the jumps without a neighboring vacancy. This effect has a dramatic impact on the theoretical predictions of the interstitial diffusion of oxygen impurities in nickel metal, as will be demonstrated in the following sections.

3.2. MD simulations of nickel lattice diffusion

In the presence of vacancies, lattice nickel atoms will occasionally jump to the nearby vacancy sites as a result of thermal agitation, a process called vacancy-mediated nickel self-diffusion. The first-principles method calculates the diffusivity based on the Eyring's reaction rate theory [84], which relates the jumping rate to the thermodynamic properties of the saddle point along the jumping path. This study attempts to predict the diffusivity theoretically by measuring the MSD within the framework of the MD simulation. The results are summarized and compared with

results reported in a previous experimental study [85] as well as first-principles predictions [86] in Fig. 5. The activation energy predicted using the lowest-vacancy-concentration (VC) data (0.1%) obtained from ReaxFF is 29.8 kcal mol^{-1}, whereas the activation energies obtained from experiment and from the QM method are 66.9 kcal mol^{-1} and 61.1 kcal mol^{-1}, respectively. The diffusivity predicted by ReaxFF is two to three orders of magnitude higher at high temperatures ($\sim$1500 K) and four to five orders of magnitude higher at low temperatures ($\sim$1000 K). Furthermore, the activation energy is underestimated by $\sim$35 kcal mol^{-1} compared with values reported in other studies.

The discrepancies among the values obtained for the diffusivity and activation energy are attributed to the non-physical vacancy concentration used in the present model, which is orders of magnitude higher than that in the real material. For instance, the equilibrium mono-vacancy concentration in nickel metal is on the order of 10^{-5} and 10^{-8} at 1500 K and 1000 K, respectively, and decreases further with decreasing temperature [87]. The present authors attempt to extrapolate their calculations to the real concentration by performing a series of calculations using high-vacancy-concentration systems, the computational cost of which is significantly lower than that of low-vacancy-concentration systems. The extrapolations at
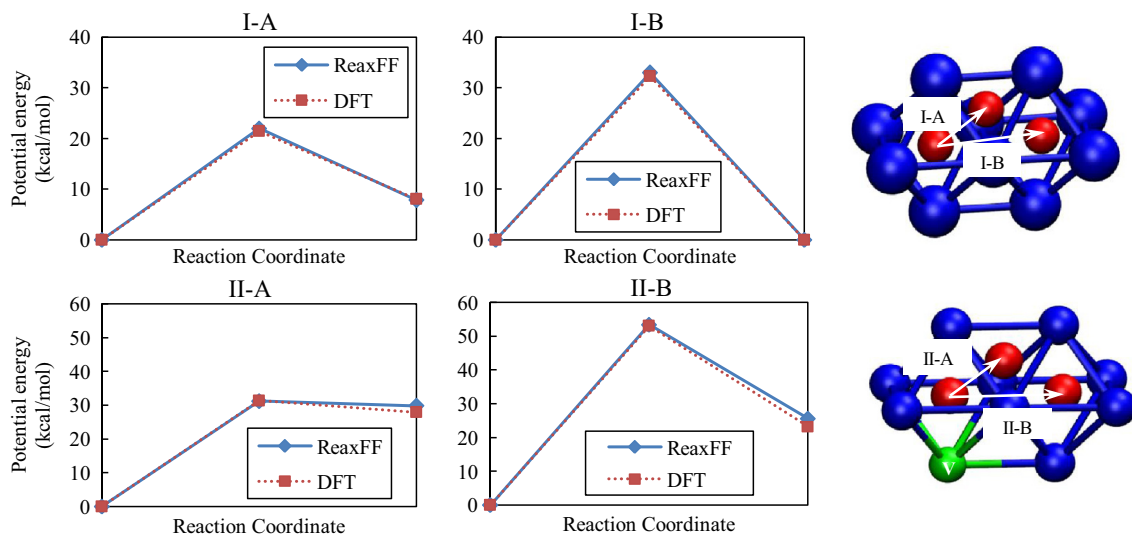

Fig. 4. Comparison of the oxygen diffusion pathway. (I-A) O–T jump without a first neighbor vacancy; (I-B) O–O jump without a first neighbor vacancy; (II-A) O–T jump with a first neighbor vacancy; (II-B) O–O jump with a first neighbor vacancy. Color code: blue, nickel atom; red, oxygen atom; green, vacancy. (For interpretation of the references to color in this figure legend, the reader is referred to the online version of this article.)
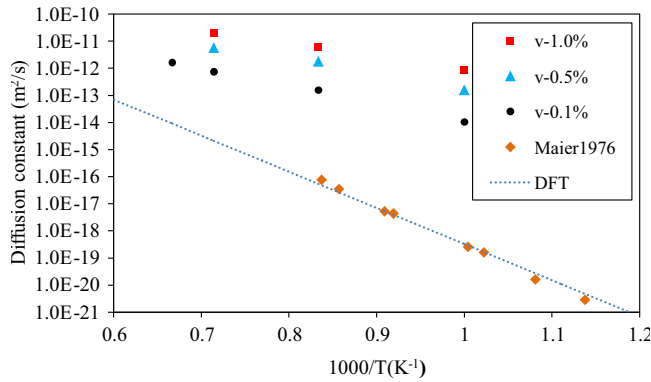
Fig. 5. Ni self-diffusion coefficient predicted from ReaxFF MD simulations in comparison with selected experimental study and first-principle calculation.

1500 K and 1000 K are demonstrated in Fig. 6, where an approximately linear relationship is observed between the diffusivity and the vacancy concentration. This relationship appears to be intuitively rational because, if the number of vacancies increases by a certain factor, the jumping rate of the lattice nickel is expected to increase by the same factor. The slope of the linear regression can be attributed to the diffusivity of vacancies rather than to the diffusivity of nickel atoms and is calculated to be 8×10^{-11} m^2 s^{-1} and 2×10^{-9} m^2 s^{-1} at 1000 K and 1500 K, respectively. Furthermore, if the VC values are estimated to be 3.0×10^{-8} and 1.2×10^{-5} at 1000 K and 1500 K, respectively, the extrapolated nickel self-diffusivity is calculated by multiplying the diffusivity of vacancies and the corresponding VC value. The resulting diffusivities are 2.4×10^{-18} m^2 s^{-1} and 2.4×10^{-14} m^2 s^{-1} at 1000 K and 1500 K, respectively. These values are in better agreement with the theoretically predicted and experimentally measured values ($\sim 10^{-19}$ m^2 s^{-1} at 1000 K and $\sim 10^{-14}$ m^2 s^{-1} at 1500 K), especially at 1500 K. The error in this extrapolation is approximately one order of magnitude at 1000 K.

The activation energy shows a similar dependence on the vacancy concentration. Using the ReaxFF MD model, the activation energy is predicted to be 22.1 kcal mol^{-1}, 25.1 kcal mol^{-1} and 29.8 kcal mol^{-1} at VC values of 1.0%, 0.5% and 0.1%, respectively. A simple extrapolation of the activation energy is not feasible, because the activation energy is measured within a certain temperature range, and the VC value is temperature dependent. However,

using the extrapolated diffusivity obtained from ReaxFF at 1000 K and 1500 K, the activation energy is estimated to be 54.9 kcal mol^{-1} based on the two data points, which is a better prediction compared with the value of 29.8 kcal mol^{-1} predicted from a fixed VC value of 0.1%. However, the error in the diffusivity at low temperature (1000 K in the present simulation) and the lack of data points from the extrapolated diffusivity (two data points in the present simulation) result in a deviation of ~ 9 kcal mol^{-1} from the activation energy predicted by other methods. A more accurate estimation of the activation energy requires multiple MD simulations of the system, which is beyond the scope of this work. Nevertheless, the measurement of the diffusivity at high VC values and the extrapolation method presented above demonstrate the applicability of the MD-based method in investigating self-diffusion in pure metallic systems.

3.3. MD simulations of oxygen diffusion

The oxygen diffusivity predicted from MD simulation is shown in Fig. 7, which compares the results obtained from diffusion simulations with and without a nearby vacancy as well as with other theoretical predictions and the most recent experimental measurements. In the case of oxygen diffusion in the perfect nickel lattice, the activation energy predicted by the present ReaxFF MD simulation is 20.1 ± 2.3 kcal mol^{-1}, which is in good agreement with the QM predicted value of 18.9 kcal mol^{-1}. The errors in the calculations of the diffusivity from MD simulations are within 50%.

For comparison, the diffusivity of oxygen in the presence of a nearby vacancy is plotted in the same figure. Owing to the large binding energy between the oxygen and the vacancy, the diffusivity of oxygen is reduced by about three orders of magnitude. Furthermore, the activation energy is predicted to be 38.3 ± 10.4 kcal mol^{-1}. The value measured experimentally by Park et al. [88] is 39.2 kcal mol^{-1}, and the value predicted by DFT is 37.8 kcal mol^{-1} [13]. The error in the measurement of the diffusivity using MD simulation is up to 70%. Relatively large errors are observed in the prediction of the activation energy. The reasons for these large errors will be discussed in the following.

Because a vacancy imposes a dramatic effect on the diffusivity and the corresponding activation energy of the interstitial oxygen atoms, the simulation trajectory is analyzed to locate the vacancy and the oxygen atom. In the diffusion simulation of an oxygen atom sitting near a vacancy,
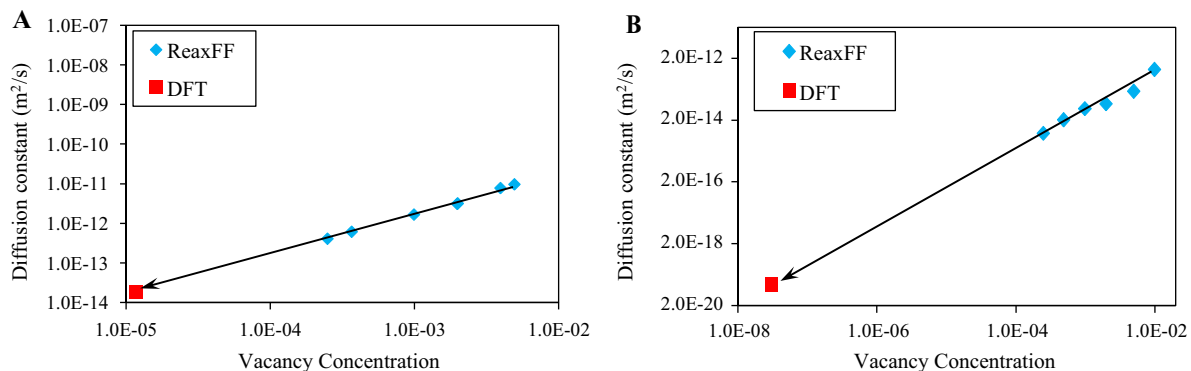

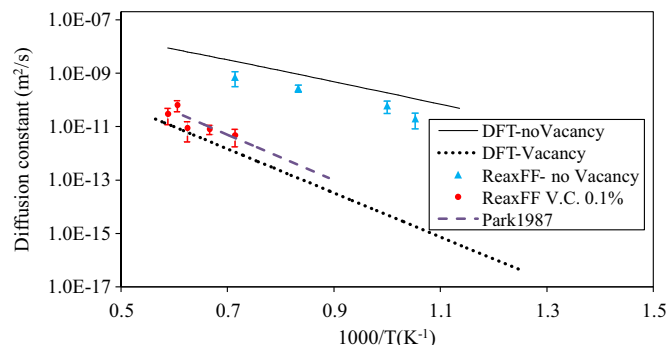**Fig. 6.** Extrapolation of the diffusivity vs. VC at: (A) 1500 K; (B) 1000 K.

Fig. 7. Oxygen diffusivity with and without a nearby vacancy in comparison with first-principles prediction and experimental measurement.

it is observed that the oxygen atom spends most of the simulation time hopping between octahedral sites surrounding the vacancy without escaping from the vacancy over the temperature range investigated. This is due to the large binding energy between the oxygen and the vacancy. This observation is reasonable, because once the oxygen escapes the vacancy, it will become an interstitial oxygen atom diffusing in the nickel matrix, and the corresponding diffusivity will be much higher than the value measured by experiment. The low diffusivity measured in the experiment indicates that it is unlikely for the oxygen to escape the vacancy.

At elevated temperatures, hopping of the vacancy–oxygen pair is observed in the MD simulation, as shown in Fig. 8. This hopping event is rare and is observed only once each at 1400 K and 1500 K. Multiple simulations starting at different initial configurations confirm that this event is detected after 1600 ps at 1400 K and between 475 and 1300 ps at 1500 K during a 2 ns MD simulation. At 1600 K, between one and three hopping events can be detected. The results of five simulations at 1600 K are summarized in Table 3. When the temperature is increased to 1650 K and 1700 K, multiple (more than five) hopping events can be detected over a period of 2 ns. The rarity of this hopping event results in the large errors in the measurements of diffusivity and activation energy. Longer simulations (lasting more than 10 ns) are expected to effectively reduce the errors associated with these calculations; however, this topic is beyond the scope of this work.
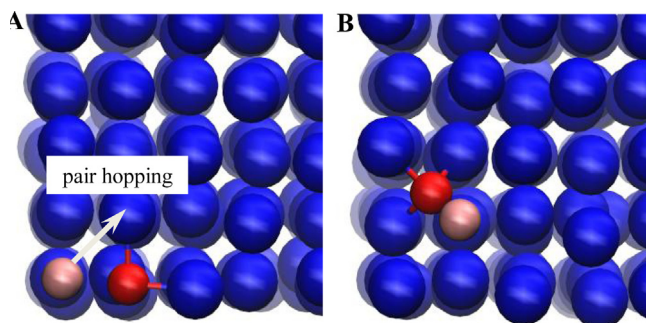
Based on the observations described above, a new oxygen diffusion mechanism is proposed, in which an oxygen atom diffuses via the movement of an "oxygen–vacancy pair". For the purpose of validation, the energy of this mechanism is compared with that of the "vacancy-modified interstitial diffusion mechanism" described in Ref. [13]; the results are shown in Fig. 9.

Fig. 9A describes the minimum energy pathway (MEP) of an oxygen atom escaping a vacancy by two elementary steps. The first step corresponds to the oxygen atom diffusing from an octahedral site (A-1 in Fig. 9) with a first nearest-neighbor vacancy to a tetrahedral site (A-2) with an energy barrier of $\sim$30 kcal mol^{-1} (A-TS$_1$). In the second step, the oxygen atom diffuses toward a nearby octahedral site (A-3), which is a stable configuration. This step crosses an energy barrier of $\sim$15 kcal mol^{-1} (A-TS$_2$). For comparison, Fig. 9B describes the MEP of the new mechanism proposed in this study, which involves three steps. The first step corresponds to an exchange between the vacancy and a first nearest-neighbor nickel atom (B-1–B-2). The barrier (B-TS$_1$) of this step is estimated using the nickel vacancy diffusion barrier, which is $\sim$35 kcal mol^{-1}. The second step is the diffusion of the oxygen toward a tetrahedral site (*B-3) with a first nearest-neighbor vacancy with an energy barrier of $\sim$15 kcal mol^{-1} (*B-TS$_2$). Finally in the third step, the oxygen atom relaxes to an octahedral site (B-4) with a first nearest-neighbor vacancy. B-3 and B-TS$_2$ are each marked by an asterisk (*) to indicate that these two data points were not included in the training process.

The overall reaction barriers of the two mechanisms are comparable, though the value of the newly proposed mechanism is $\sim$5 kcal mol^{-1} smaller. In addition, this mechanism is thermodynamically favored, because it leads to a more stable configuration of the interstitial oxygen atom. Furthermore, the backward reaction of A-2 to A-1 experiences a barrier of $\sim$5 kcal mol^{-1}. This low barrier makes the further escape of the oxygen atom kinetically hindered: a "half-way" escaped oxygen atom will quickly migrate

Fig. 8. System snapshot during the MD simulation of oxygen diffusion at 1500 K: (A) initial configuration; (B) configuration at 875 ps. Color code: blue, nickel atom; red, oxygen atom; pink, vacancy; hopping direction indicated by gray arrow. (For interpretation of the references to color in this figure legend, the reader is referred to the online version of this article.)

Table 3. Details of the hopping events of the vacancy-oxygen pair at 1600 K.

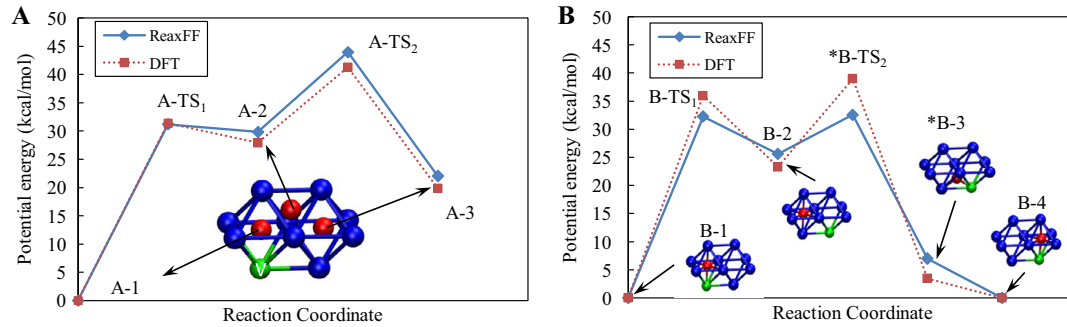| Trial simulation	Hopping events detected	Time of occurrence (ps)
1	3	125/1000/1319
2	1	1450
3	2	340/410
4	2	150/1225
5	1	200

Fig. 9. Comparison of the two oxygen diffusion mechanisms: (A) vacancy-modified interstitial diffusion mechanism; (B) vacancy–oxygen pair diffusion mechanism. Color code: blue, nickel atom; red; oxygen atom; green, vacancy. TS, transition state. [*] Data point not included in the training set. (For interpretation of the references to color in this figure legend, the reader is referred to the online version of this article.)

back to the A-1 state. This low barrier is why the escape of oxygen atoms was not observed in the MD simulation. In contrast, the newly proposed mechanism finds a metastable intermediate state (B-2), the forward and backward diffusion barriers of which are comparable. The forward process from the B-2 state contributes to the diffusivity of the oxygen atom.

Because the first step of this new mechanism is the vacancy-mediated self-diffusion of nickel, the competing backward reaction (B-2–B-1) is expected to decrease the diffusivity of nickel. To test this hypothesis, the diffusivity of nickel is calculated by performing an MD simulation of a system containing an oxygen–vacancy pair and comparing the result with that obtained from a system containing no interstitial oxygen atoms. The results are shown in Fig. 10. The reason for the observed decrease in the diffusivity of nickel is attributed to the lower effective jumping rate due to the presence of the oxygen–vacancy pair.

The foregoing discussion demonstrates the validity of the newly proposed oxygen diffusion mechanism. Garruchet et al. [26] proposed a vacancy mechanism based on VCMD simulation. In that study, the authors also demonstrated the effect of vacancies on the diffusivity of oxygen atoms. However, the authors claimed that the diffusivity of oxygen will be higher at higher VC values. Similar tests were performed at higher VC values (0.2%, 0.4% and 0.8%, in addition to 0.1%) in this study at 1500 K, and the results are shown in Fig. 11. In the simulation involving a VC value of 0.2%, two jumps of the oxygen–vacancy pair were observed at

~175 ps and ~400 ps. At 0.4% VC, one jump was detected at ~675 ps. These results agree with the observations at a VC value of 0.1%. Interestingly, however, It was observed that, at 0.8% VC, the oxygen detached from the vacancy and became an interstitial oxygen atom. The resulting diffusivity is on the order of 10^{-9} m^2 s^{-1}, which agrees with the diffusivity of oxygen measured in the absence of a vacancy in the MD simulation. The exact mechanism of this detachment is uncertain: it might be due to the effect of an unphysically high VC value or a rare event as a result of thermal agitation. Furthermore, no clear, positive effect of the VC value was observed on the diffusivity of oxygen in the range of VC values investigated at least at 1500 K. This finding is valid when the concentrations of oxygen atoms and vacancies are both low. In a dilute solution, an oxygen–vacancy pair is unlikely to meet another vacancy, and the interactions between vacancies are negligible. The increase in the diffusivity of oxygen with an increase in the VC value in Ref. [26] remains within one order of magnitude, which is within the error of the MD study.

3.4. MD simulation of vacancy-induced oxidation initiation

Vacancies have been shown to have a strong binding effect on oxygen atoms. Recent experiments indicate that the vacancies formed at the metal–oxide interface by outward cation diffusion during oxidation can be injected into the metal and annihilate at the GB to form a void [89]. Furthermore, the walls of the voids are observed to be
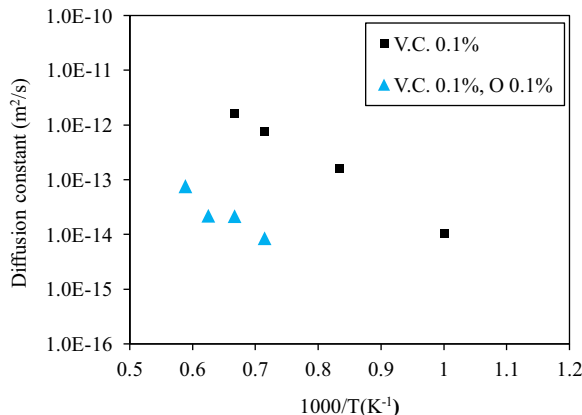

Fig. 10. Effect of an interstitial oxygen atom on the vacancy-mediated self-diffusion of nickel.
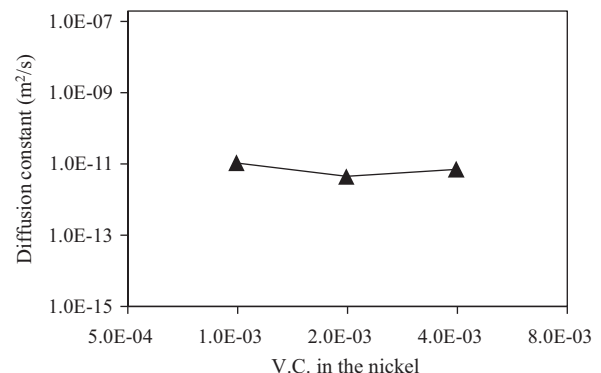

Fig. 11. Oxygen diffusivity at 1500 K as a function of VC value in nickel.
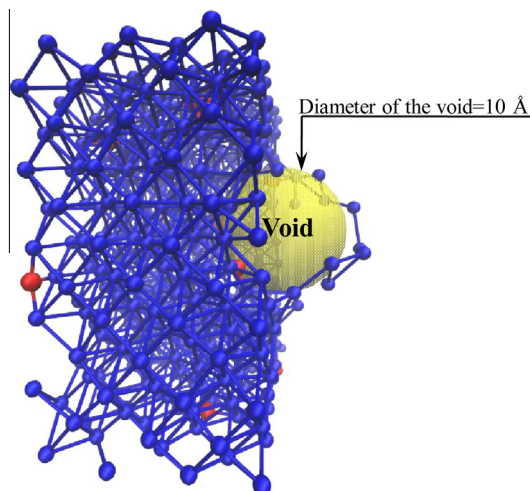
Fig. 12. Cross-section view of the system initial configuration for oxidation simulation. Color code: blue, nickel atom; red, oxygen atom; yellow, void region. (For interpretation of the references to color in this figure legend, the reader is referred to the online version of this article.)

Fig. 14. Number of oxygen atoms in the core region (5 Å radius to the center of the simulation box) as a function of simulation time.

oxidized, with the voids corresponding to NiO particles [9]. The present authors attempted to study this phenomenon using MD simulation. An fcc Ni $6 \times 6 \times 6$ super cell was expanded from the unit cell by replicating the cell in all three dimensions. A void with a diameter of 10 Å was created, with its center located at the center of the super cell by removing all the metal atoms within this range. The resulting structure was then annealed at 1500 K. Lastly, 23 oxygen atoms were randomly inserted in the nickel matrix. The coordinates of insertion were biased so that no oxygen atom was inserted within 5 Å of the center (the void region). The resulting nickel matrix with randomly inserted oxygen atoms was annealed again at 1500 K and subjected to NVT simulations at 1500 K for 200 ps. A depiction of this model is provided in Fig. 12, where the cross section of the super cell is shown.

Three snapshots during the evolution of the system at different times are shown in Fig. 13. The number of oxygen atoms entering the core region was monitored during the simulation, and the result is shown in Fig. 14. Approximately three oxygen atoms entered the core region during the annealing process. The following NVT simulation showed a steady growth in the number of oxygen atoms within the core region up to 50 ps, reaching a total of 11
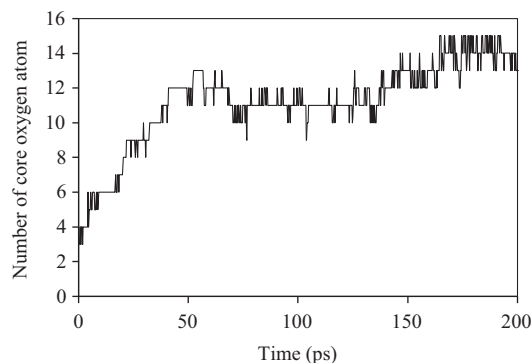
atoms. Then, no more oxygen atoms entered the region until 130 ps. At the end of the simulation, the number of oxygen atoms within the core region reached 13.

Furthermore, the charge on the nickel atoms was compared before and after the simulation, as shown in Fig. 15. Each dot in the figure represents a nickel atom. The *y*-axis denotes the charge on the nickel atoms, and the *x*-axis marks the distance from the corresponding nickel atom to the center of the super cell. At the beginning of the simulation, most of the nickel atoms carried zero charge, indicating a metallic environment. The red dots above the zero charge indicate that the initial charge on the nickel atoms ranged from +0.1 to +0.5, owing to charge transfer between the nickel atoms and the oxygen atoms. The charge distribution after the simulation is represented by the black dots. The majority of the nickel atoms retained zero charge. However, a portion of nickel atoms entered the core region with a charge ranging between +0.5 and +0.8, as indicated by the black dots distributed in the upper left corner of Fig. 15.

The number of oxygen atoms entered the core region, and the charges on the nickel atoms verify the enrichment of oxygen in the core region and the tendency to form nickel oxide. Owing to the relatively short time scale described by the MD simulations, the nickel oxide in the core region is amorphous in nature, and it is difficult to observe the crystallization process. However, this MD simulation demonstrates the strong tendency of vacancies to bind with oxygen and the corresponding effect on the internal oxidation of nickel. The void formed at the GB by the injection of vacancies at the metal–oxide interface has a
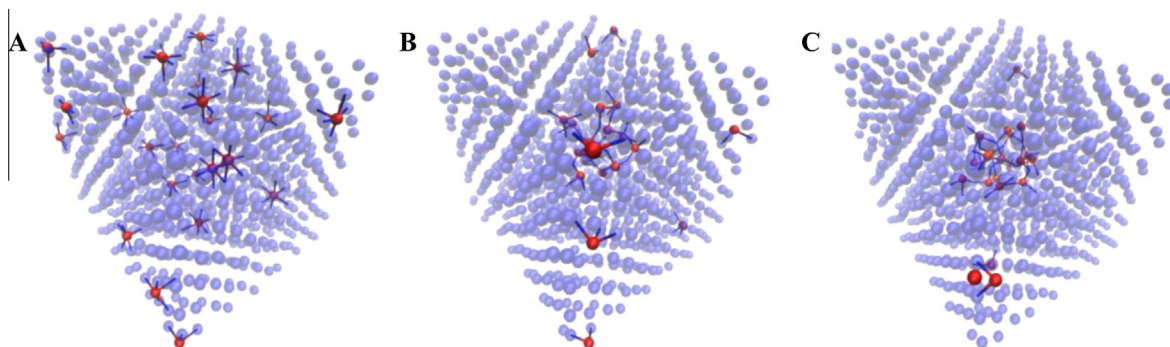

Fig. 13. System snapshots during the internal oxidation simulation at: (A) 0 ps; (B) 50 ps; (C) 200 ps. Color code: transparent blue, nickel atom; red, oxygen. (For interpretation of the references to color in this figure legend, the reader is referred to the online version of this article.)
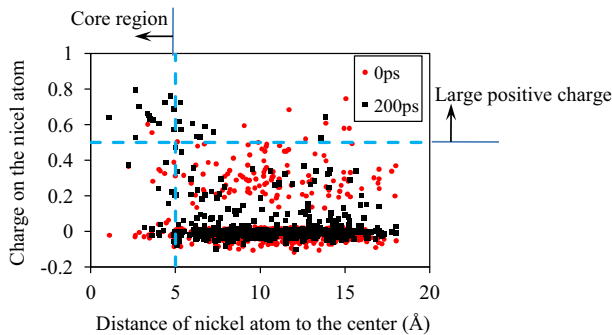
Fig. 15. Comparison of the atomic charge on the nickel atoms between the initial and final configuration as a function of distance to the center of the structure.

cumulative effect on the oxygen atoms that are diffusing along the GB. The enrichment of the local oxygen concentration near a void will lead to the formation of a nickel oxide particle, as observed in the experimental studies.

The source of oxygen atoms forming the oxide at GB remains an open question. Perusin et al. [9] suggested the possibility of GB diffusion of oxygen. Based on the diffusion simulation described in the previous section, it is also possible that the lattice oxygen atoms are stabilized by vacancies in nickel grains. The resulting oxygen–vacancy pair will diffuse and ultimately annihilate at a defect in the GB. The large numbers of vacancies that originate at the metal–oxide interface as a result of the outward cation diffusion serve as a medium for the oxygen transport in the metal grains.

4. Conclusions

A ReaxFF reactive force field was developed for the Ni/O system, to study the diffusion and internal oxidation of nickel. The vacancy-mediated self-diffusion of nickel predicted by measuring the MSD is in good agreement with data published in the literature. In addition, the presence of vacancies is demonstrated to strongly affect the stability and mobility of interstitial oxygen atoms. Based on the results of the MD simulation, a new mechanism of oxygen diffusion is proposed, in which dissolved oxygen atoms diffuse via the movement of oxygen–vacancy pairs. Furthermore, with this force field, the oxide nucleation initiated by a defect inside a grain was simulated. It was observed that the void inside the grain will stabilize the diffusing oxygen atoms. The enrichment of the local oxygen concentration will initiate the internal oxidation of nickel. The diffusion simulations suggest the possibility of grain oxygen transportation via vacancy movement.

Acknowledgement

References

[1] C. Cabet, F. Rouillard, J. Eng. Gas Turbines Power Trans. ASME (2009) 131.
[2] T.M. Pollock, S. Tin, J. Propul. Power 22 (2006) 361.
[3] D. Furrer, H. Fecht, JOM J. Miner. Met. Mater. Soc. 51 (1999) 14.
[4] R. Arunachalam, M.A. Mannan, Mach. Sci. Technol. 4 (2000) 127.
[5] R. Haugsrud, Corros. Sci. 45 (2003) 211.
[6] R.H. Bricknell, D.A. Woodford, Metall. Mater. Trans. A 12 (1981) 425.
[7] D.A. Woodford, R.H. Bricknell, Metall. Mater. Trans. A 12 (1981) 1467.
[8] R.H. Bricknell, D.A. Woodford, Acta Metall. 30 (1982) 257.
[9] S. Perusin, D. Monceau, E. Andrieu, J. Electrochem. Soc. 152 (2005) E390.
[10] C. Wert, C. Zener, Phys. Rev. 76 (1949) 1169.
[11] E.H. Megchiche, M. Amarouche, C. Mijoule, J. Phys. Condens. Matter (2007) 19.
[12] J.J. Kim, S.H. Shin, J.A. Jung, K.J. Choi, J.H. Kim, Appl Phys Lett (2012) 100.
[13] H.Z. Fang, S.L. Shang, Y. Wang, Z.K. Liu, D. Alfonso, D.E. Alman, et al., J. Appl. Phys. 115 (2014) 043501.
[14] H.O. Nam, I.S. Hwang, K.H. Lee, J.H. Kim, Corros. Sci. 75 (2013) 248.
[15] N. Jakse, A. Pasturel, J. Chem. Phys. 120 (2004) 6124.
[16] J.P.K. Doye, D.J. Wales, New J. Chem. 22 (1998) 733.
[17] M.S. Daw, M.I. Baskes, Phys. Rev. B 29 (1984) 6443.
[18] S.M. Foiles, M.I. Baskes, M.S. Daw, Phys. Rev. B 33 (1986) 7983.
[19] S.S. Hayat, M.A. Choudhry, S.A. Ahmad, J.I. Akhter, A. Hussain, Indian J. Pure Appl. Phys. 46 (2008) 771.
[20] X.W. Zhou, H.N.G. Wadley, J. Phys. Condens. Matter 17 (2005) 3619.
[21] A. Perron, S. Garruchet, O. Politano, G. Aral, V. Vignal, J. Phys. Chem. Solids 71 (2010) 119.
[22] A. Hasnaoui, O. Politano, J.M. Salazar, G. Aral, Phys. Rev. B (2006) 73.
[23] S.K.R.S. Sankaranarayanan, S. Ramanathan, Phys. Rev. B (2008) 78.
[24] B. Jeon, S. Sankaranarayanan, S. Ramanathan, J. Phys. Chem. C 115 (2011) 6571.
[25] S. Garruchet, O. Politano, P. Arnoux, V. Vignal, Appl. Surf. Sci. 256 (2010) 5968.
[26] S. Garruchet, O. Politano, P. Arnoux, V. Vignal, Solid State Commun. 150 (2010) 439.
[27] A. Elsener, O. Politano, P.M. Derlet, H. Van Swygenhoven, Modell. Simul. Mater. Sci. Eng. (2008) 16.
[28] A. Elsener, O. Politano, P.M. Derlet, H. Van Swygenhoven, Acta Mater. 57 (2009) 1988.
[29] A.C.T. van Duin, S. Dasgupta, F. Lorant, W.A. Goddard III, J. Phys. Chem. A 105 (2001) 9396.
[30] J.A. Keith, D. Fantauzzi, T. Jacob, A.C.T. van Duin, Phys. Rev. B (2010) 81.
[31] W.J. Mortier, S.K. Ghosh, S. Shankar, J. Am. Chem. Soc. 108 (1986) 4315.
[32] G.O.A. Janssens, B.G. Baekelandt, H. Toufar, W.J. Mortier, R.A. Schoonheydt, J. Phys. Chem. 99 (1995) 3251.
[33] F.H. Streitz, J.W. Mintmire, Phys. Rev. B 50 (1994) 11996.
[34] M.F. Russo Jr., R. Li, M. Mench, A.C.T. van Duin, Int. J. Hydrogen Energy 36 (2011) 5828.
[35] K.L. Joshi, A.C.T. van Duin, Energy Fuels 27 (2013) 4481.
[36] A.C.T. van Duin, A. Strachan, S. Stewman, Q.S. Zhang, X. Xu, W.A. Goddard, J. Phys. Chem. A 107 (2003) 3803.
[37] T.T. Jarvi, A. Kuronen, M. Hakala, K. Nordlund, A.C.T. van Duin, W.A. Goddard III, et al., Eur. Phys. J. B 66 (2008) 75.
[38] Y.K. Shin, H. Kwak, C.Y. Zou, A.V. Vasenkov, A.C.T. van Duin, J. Phys. Chem. A 116 (2012) 12163.
[39] O. Verners, Y.K. Shin, A.C.T. van Duin, J. Appl. Phys. (2013) 114.
[40] J.G.O. Ojwang, R. van Santen, G.J. Kramer, A.C.T. van Duin, W.A. Goddard III, J. Chem. Phys. (2008) 129.
[41] C.Y. Zou, A.C.T. van Duin, D.C. Sorescu, Top Catal. 55 (2012) 391.

[42] J.G.O. Ojwang, R. van Santen, G.J. Kramer, A.C.T. van Duin, W.A. Goddard III, J. Chem. Phys. 128 (2008) 164714.

[43] S.-Y. Kim, N. Kumar, P. Persson, J. Sofo, A.C.T. van Duin, J.D. Kubicki, Langmuir 29 (2013) 7838.

[44] J.G.O. Ojwang, R.A. van Santen, G.J. Kramer, A.C.T. van Duin, W.A. Goddard III, J. Chem. Phys. (2009) 131.

[45] S. Cheung, W.-Q. Deng, A.C.T. van Duin, W.A. Goddard III, J. Phys. Chem. A 109 (2005) 851.

[46] T.P. Senftle, R.J. Meyer, M.J. Janik, A.C.T. van Duin, J. Chem. Phys. (2013) 139.

[47] M. Aryanpour, A.C.T. van Duin, J.D. Kubicki, J. Phys. Chem. A 114 (2010) 6298.

[48] D. Raymand, A.C.T. van Duin, M. Baudin, K. Hermansson, Surf. Sci. 602 (2008) 1020.

[49] K. Chenoweth, A.C.T. van Duin, W.A. Goddard III, J. Phys. Chem. A 112 (2008) 1040.

[50] G. Yan, Z. Zhang, K. Yan, Mol. Phys. 111 (2013) 147.

[51] X.M. Cheng, Q.D. Wang, J.Q. Li, J.B. Wang, X.Y. Li, J. Phys. Chem. A 116 (2012) 9811.

[52] C.Y. Zou, S. Raman, A.C.T. van Duin, J. Phys. Chem. B 118 (2014) 6302.

[53] K. Chenoweth, A.C.T. van Duin, S. Dasgupta, W.A. Goddard III, J. Phys. Chem. A 113 (2009) 1740.

[54] J.P. Leininger, C. Minot, F. Lorant, Theochem. J. Mol. Struct. 852 (2008) 62.

[55] E. Salmon, A.C.T. van Duin, F. Lorant, P.M. Marquaire, W.A. Goddard, Org. Geochem. 40 (2009) 416.

[56] J. Ding, L. Zhang, Y. Zhang, K.-L. Han, J. Phys. Chem. A 117 (2013) 3266.

[57] M. Zheng, X. Li, J. Liu, L. Guo, Energy Fuels 27 (2013) 2942.

[58] K. Chenoweth, A.C.T. van Duin, P. Persson, M.-J. Cheng, J. Oxgaard, W.A. Goddard III, J. Phys. Chem. C (2008).

[59] J.E. Mueller, A.C.T. van Duin, W.A. Goddard III, J. Phys. Chem. C 114 (2010) 4939.

[60] C.Y. Zou, A.C.T. van Duin, JOM 64 (2012) 1426.

[61] S.G. Srinivasan, A.C.T. van Duin, J. Phys. Chem. A 115 (2011) 13269.

[62] M.M. Islam, V.S. Bryantsev, A.C.T. van Duin, J. Electrochem. Soc. 161 (2014) 3009.

[63] D.-C. Yue, T.-B. Ma, Y.-Z. Hu, J. Yeon, A.C.T. van Duin, H. Wang, et al., J. Phys. Chem. C 117 (2013) 25604.

[64] C.H. Lee, J.-H. Kim, C. Zou, I.S. Cho, J.M. Weisse, W. Nemeth, et al., Sci. Rep. (2013) 3.

[65] O. Assowe, O. Politano, V. Vignal, P. Arnoux, B. Diawara, O. Verners, et al., J. Phys. Chem. A 116 (2012) 11796.

[66] G. Kresse, J. Furthmuller, Phys. Rev. B 54 (1996) 11169.

[67] G. Kresse, J. Furthmuller, Comput. Mater. Sci. 6 (1996) 15.

[68] G. Kresse, D. Joubert, Phys. Rev. B 59 (1999) 1758.

[69] J.P. Perdew, A. Zunger, Phys. Rev. B 23 (1981) 5048.

[70] J. Tersoff, Phys. Rev. B 37 (1988) 6991.

[71] D.W. Brenner, Phys. Rev. B 42 (1990) 9458.

[72] K.-I. Nomura, R.K. Kalia, A. Nakano, P. Vashishta, A.C.T. van Duin, W.A. Goddard III, Phys. Rev. Lett. (2007) 99.

[73] H.-P. Chen, R.K. Kalia, E. Kaxiras, G. Lu, A. Nakano, K.-I. Nomura, et al., Phys. Rev. Lett. (2010) 104.

[74] K.L. Joshi, S. Raman, A.C.T. van Duin, J. Phys. Chem. Lett. 4 (2013) 3792.

[75] S. Plimpton, J. Comput. Phys. 117 (1995) 1.

[76] A.C.T. van Duin, J.M.A. Baas, B. van de Graaf, J. Chem. Soc. Faraday Trans. 90 (1994) 2881.

[77] A. Einstein, Ann. Phys. 17 (1905) 549.

[78] H.J.C. Berendsen, J.P.M. Postma, W.F. Vangunsteren, A. Dinola, J.R. Haak, J. Chem. Phys. 81 (1984) 3684.

[79] T.B. Massalski, Binary Alloy Phase Diagrams, ASM International, Materials Park, OH, 1990.

[80] P.S. Maiya, J.M. Blakely, J. Appl. Phys. 38 (1967) 698.

[81] W.R. Tyson, W.A. Miller, Surf. Sci. 62 (1977) 267.

[82] E.H. Megchiche, S. Perusin, J.-C. Barthelat, C. Mijoule, Phys. Rev. B (2006) 74.

[83] S. Ganeshan, L.G. Hector Jr., Z.K. Liu, Acta Mater. 59 (2011) 3214.

[84] H. Eyring, J. Chem. Phys. 3 (1935) 107.

[85] K. Maier, H. Mehrer, E. Lessmann, W. Schule, Phys. Status Solidi B 78 (1976) 689.

[86] C.Z. Hargather, S.L. Shang, Z.K. Liu, Y. Du, Comput. Mater. Sci. 86 (2014) 17.

[87] M. De Koning, S.B.R. De Debiaggi, A.M. Monti, Defect Diffus. Forum 224/225 (2004) 59.

[88] J.W. Park, C.J. Altstetter, Metall. Mater. Trans. A 18 (1987) 43.

[89] S. Perusin, B. Viguier, D. Monceau, L. Ressier, E. Andrieu, Acta Mater. 52 (2004) 5375.